

## Mechanisms of broadband noise generation on metal foam edges

Rubio Carpio, Alejandro; Avallone, Francesco; Ragni, Daniele; Snellen, Mirjam; Van Der Zwaag, Sybrand

**DOI**

[10.1063/1.5121248](https://doi.org/10.1063/1.5121248)

**Publication date**

2019

**Document Version**

Final published version

**Published in**

Physics of Fluids

**Citation (APA)**

Rubio Carpio, A., Avallone, F., Ragni, D., Snellen, M., & Van Der Zwaag, S. (2019). Mechanisms of broadband noise generation on metal foam edges. *Physics of Fluids*, 31(10), Article 105110. <https://doi.org/10.1063/1.5121248>

**Important note**

To cite this publication, please use the final published version (if applicable).  
Please check the document version above.

**Copyright**

Other than for strictly personal use, it is not permitted to download, forward or distribute the text or part of it, without the consent of the author(s) and/or copyright holder(s), unless the work is under an open content license such as Creative Commons.

**Takedown policy**

Please contact us and provide details if you believe this document breaches copyrights.  
We will remove access to the work immediately and investigate your claim.

# Mechanisms of broadband noise generation on metal foam edges

Cite as: Phys. Fluids **31**, 105110 (2019); <https://doi.org/10.1063/1.5121248>

Submitted: 23 July 2019 . Accepted: 06 October 2019 . Published Online: 24 October 2019

Alejandro Rubio Carpio , Francesco Avallone , Daniele Ragni , Mirjam Snellen, and Sybrand van der Zwaag 

## COLLECTIONS

Paper published as part of the special topic on [Special Topic on Passive and Active Control of Turbulent Flows](#)

Note: This paper is part of the Special Topic on Passive and Active Control of Turbulent Flows.



This paper was selected as Featured



View Online



Export Citation



CrossMark

## ARTICLES YOU MAY BE INTERESTED IN

[Optimization under turbulence model uncertainty for aerospace design](#)

Physics of Fluids **31**, 105111 (2019); <https://doi.org/10.1063/1.5118785>


[Effective viscoelasticity of non-Newtonian fluids modulated by large-spherical particles aligned under unsteady shear](#)

Physics of Fluids **31**, 103304 (2019); <https://doi.org/10.1063/1.5119335>

[Deformation of a vortex ring caused by its impingement on a sphere](#)

Physics of Fluids **31**, 107108 (2019); <https://doi.org/10.1063/1.5122260>

CAPTURE WHAT'S POSSIBLE  
WITH OUR NEW PUBLISHING ACADEMY RESOURCES

Learn more 



# Mechanisms of broadband noise generation on metal foam edges

Cite as: Phys. Fluids 31, 105110 (2019); doi: 10.1063/1.5121248

Submitted: 23 July 2019 • Accepted: 6 October 2019 •

Published Online: 24 October 2019



Alejandro Rubio Carpio,<sup>a)</sup>  Francesco Avallone,  Daniele Ragni,  Mirjam Snellen, and Sybrand van der Zwaag 

## AFFILIATIONS

Faculty of Aerospace, Delft University of Technology, Kluyverweg 1, 2629 HS Delft, The Netherlands

**Note:** This paper is part of the Special Topic on Passive and Active Control of Turbulent Flows.

<sup>a)</sup>Electronic mail: [a.rubiocarpio@tudelft.nl](mailto:a.rubiocarpio@tudelft.nl)

## ABSTRACT

The turbulent flow over a porous trailing edge of a NACA 0018 airfoil is experimentally investigated to study the link between the hydrodynamic flow field and the acoustic scattering. Four porous trailing edges, obtained from open-cell metal foams, are tested to analyze the effects on far-field noise of the permeability of the material and of the hydrodynamic communication between the two sides of the airfoil. The latter is assessed by filling the symmetry plane of two of the porous trailing edges with a thin layer of adhesive that acts as a solid membrane. Experiments are performed at a zero degree angle of attack. Far-field noise measurements show that the most permeable metal foam reduces noise (up to 10 dB) with respect to the solid trailing edge for Strouhal numbers based on the chord below 16. At higher nondimensional frequencies, a noise increase is measured. The porous inserts with an adhesive layer show no noise abatement in the low frequency range, but only a noise increase at higher frequency. The latter is, therefore, attributed to surface-roughness noise. Flow field measurements, carried out with time-resolved planar particle image velocimetry, reveal correlation of near-wall velocity fluctuations between the two sides of the permeable trailing edges only within the frequency range where noise abatement is reported. This flow communication suggests that permeable treatments abate noise by distributing the impedance jump across the foam in the streamwise direction, promoting noise scattering from different chordwise locations along the inserts. This is further confirmed by noise source maps obtained from acoustic beamforming. For the frequency range where noise reduction is measured, the streamwise position of the main noise emission depends on the permeability of the insert. At higher frequencies, noise is scattered from upstream the trailing edge independently of the test case, in agreement with the roughness-generated noise assumption.

Published under license by AIP Publishing. <https://doi.org/10.1063/1.5121248>

## I. INTRODUCTION

Broadband trailing-edge noise, generated by the scattering of turbulent structures at the trailing edge of lifting devices,<sup>1,2</sup> is the dominant noise source in wind turbines.<sup>3,4</sup> Because of stringent noise regulations, particularly close to urban areas, it also represents a limit to power production.<sup>5</sup> Extensive research has been performed to reduce this noise source through the modification of the geometry of the edge, e.g., with the use of serrations,<sup>6–10</sup> combed-serrations,<sup>11</sup> brushes,<sup>12,13</sup> or the modification of the incoming boundary layer flow, e.g., with the application of finlets<sup>14</sup> or trailing edge blowing.<sup>15,16</sup>

Recently, it has been shown that it is possible to further reduce broadband noise with respect to the previous solutions by installing porous materials at the trailing edge.<sup>17–19</sup> This passive noise

control method has shown broadband noise reduction up to 24 dB with respect to a baseline, fully solid airfoil.<sup>20</sup> Previous experimental works<sup>21</sup> have identified the flow permeability and pore size as the most relevant parameters that affect the scattered noise. In more detail, an increase in permeability results in a larger low-frequency noise reduction, while a larger pore diameter increases the noise at high-frequency with respect to a solid edge. Yet, porous treatments also reduce the aerodynamic performance of the airfoil, i.e., decrease lift and increase drag, which is enhanced by the employment of materials with higher permeability.<sup>22</sup> The choice of an optimal chordwise extension and type of porous treatment is thus a trade-off between aerodynamic and acoustic performance, which requires a full understanding of the noise generation mechanisms that has not been achieved yet.

Previous investigations showed significant differences between the noise generation mechanisms for a solid and porous trailing edge. The analysis of the acoustic scattering of a gust convecting over a partially permeable airfoil<sup>23</sup> or a solid flat plate with porous extension<sup>24</sup> suggests that a secondary noise source appears at the discontinuity between the solid body and the porous treatment; in addition, noise scattering at the trailing edge is decreased by a pressure balance process, which lowers the magnitude of the acoustic impedance jump. These two findings suggest that the theory used for predicting noise for a solid trailing edge is not directly applicable to a porous trailing edge. This was also confirmed experimentally. For example, for a porous trailing edge, an increase in the boundary layer thickness or the intensity of the turbulent fluctuations close to the edge may result in noise reduction,<sup>25</sup> different than what is expected for a solid edge.<sup>26</sup> In addition, experiments carried out in different facilities<sup>20,27,28</sup> have shown different power laws for the scaling of the far-field acoustic pressure, i.e., ranging between the 5th and the 7th power of the Mach number, while the analytical solution<sup>29</sup> reports a dipolelike dependence to the power of 6. These discrepancies might be related to the different materials adopted.

This study is aimed at finding experimental evidence of the pressure balance process described by Delfs *et al.*<sup>23</sup> Given that characterizing the flow inside metal foam inserts would compromise its nature, this study focuses on revealing the unsteady flow connection between the two sides of the airfoil through the permeable media. This will be referred to as cross-flow in the remainder of this paper. To better define the link between the flow within permeable trailing edges and the mitigation of the pressure jump at the edge (hence, far-field noise emission), two sets of metal foam inserts and a baseline (solid) trailing edge are investigated. The first set consists of two fully permeable inserts with different flow permeability, while the second one is obtained from the same materials by filling the symmetry plane with adhesive, thus avoiding flow communication between the two sides of the airfoil. The dominant noise sources are analyzed by using noise source imaging with acoustic beamforming, and the turbulent flow field is characterized with an optical nonintrusive method, i.e., Particle Image Velocimetry (PIV). Measurements are performed on a NACA 0018 airfoil at a chord-based Reynolds number  $Re_c$  of  $2.63 \times 10^5$ . To prevent steady flow from flowing through the foam inserts, the airfoil is set at zero degree angle of attack.

The remainder of this article is structured as follows: The experimental setup and data reduction procedure are described in Sec. II. Far-field acoustic scattering is shown in Sec. III. The appearance of correlation between turbulent motions around porous inserts, as well as the implications on the scattered noise, is addressed in Sec. IV. The change in the position of dominant sound sources within the metal foam inserts is discussed in Sec. V. Finally, Sec. VI reports the conclusions of this manuscript.

## II. EXPERIMENTAL APPARATUS AND DATA PROCESSING

### A. Wind tunnel and model

Experiments are performed in the A-Tunnel, the anechoic vertical low-turbulence open-jet wind tunnel at Delft University of Technology. The tunnel has a rectangular test section ( $40 \times 70 \text{ cm}^2$ )

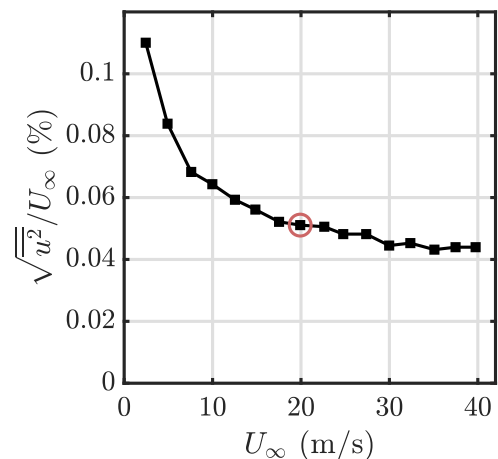


FIG. 1. Turbulence intensity  $\sqrt{u^2}/U_\infty$  as a function of the free-stream velocity  $U_\infty$  at the center of the nozzle exit. The test condition for the current investigation is marked by the red circle.

and a contraction ratio of 15:1. At the selected free-stream velocity  $U_\infty = 20 \text{ m s}^{-1}$ , the velocity distribution is uniform within 0.5% across the test section and the turbulence intensity  $\sqrt{u^2}/U_\infty$  is approximately 0.05% (Fig. 1). For the turbulence intensity characterization, a single-wire Dantec Dynamics P11 probe (platinum-plated tungsten wire with  $5 \mu\text{m}$  diameter and 1.25 mm length), connected to a TSI IFA-300 constant-temperature Wheatstone bridge, is employed at the center of the nozzle exit, and data are bandpass filtered between 20 Hz and 20 kHz.

A NACA 0018 airfoil [Figs. 2(a) and 2(b)] with chord  $c$  of 0.2 m and span  $L$  of 0.4 m is employed. The leading edge of the model is placed at 50 cm from the contraction outlet. The trailing-edge thickness is 0.3 mm to avoid blunt trailing-edge noise within the measured frequency range. The model is placed between two wooden side plates (with height of 1.2 m) flush mounted to the nozzle exit. The side plates support the model, guarantee optical access, and keep the incoming flow two-dimensional. The airfoil is manufactured with computer numerical control machining using aluminum,

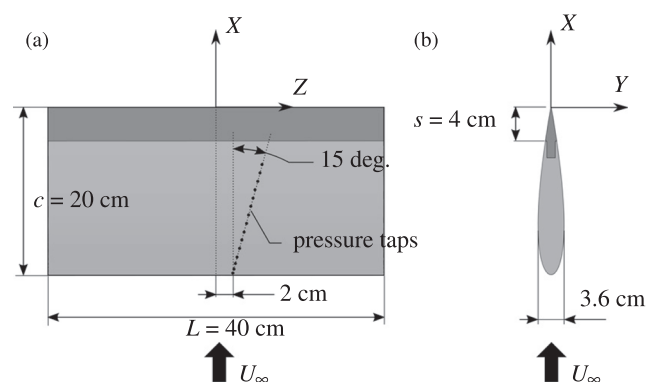


FIG. 2. Sketch of the model. The aluminum body and the metal foam insert are depicted in light and dark gray, respectively. (a) Top view. (b) Side view.

yielding a nominal surface roughness of 0.05 mm. The last 20% of the chord ( $s = 4$  cm) is interchangeable, hence allowing for testing different materials. A sketch of the streamwise-vertical  $X$ - $Y$ - $Z$  coordinate system, used for the description of the experimental setup, is also included in Figs. 2(a) and 2(b). The coordinate system has its origin at the intersection between the trailing edge line and the midspan plane of the airfoil, and the  $X$  and  $Z$ -axis are aligned with the chord and the trailing edge, respectively.

Boundary layer transition to a turbulent state is forced at 20% of the chord ( $X/c = -0.8$ ) on both sides of the airfoil using a 10 mm strip with carborundum particles of 0.84 mm diameter randomly distributed along the span. The homogeneity of the turbulence downstream the turbulator is assessed with an amplified stethoscope probe<sup>30</sup> [composed of a Brüel & Kjaer (B&K) 4134 microphone and a B&K 2619 preamplifier]. The ratio of airfoil thickness to jet width is equal to 0.05; only minor blockage effects are thus expected.<sup>31</sup> This is confirmed by measuring the static pressure distribution along the chord of the airfoil at an angle of attack of  $4.8^\circ$ ; results (not shown here for the sake of brevity) reveal a suction peak close to the nose, equivalent to that of an airfoil in free-air conditions.<sup>32</sup>

Finally, the five different trailing-edge mock-ups used in the study are described. The first one is solid, entirely manufactured in aluminum and used as reference. The metal foam inserts are all manufactured using electrical discharge machining. Two different *Alantum* NiCrAl homogeneous open-cell metal foams, with nominal cell diameter  $d_c$  of 450 and 800  $\mu\text{m}$ , are employed in this investigation. They are characterized in terms of porosity  $\sigma$ , permeability  $K$ , resistivity  $R$ , and form coefficient  $C$ ; a summary of these properties is presented in Table I. The reader can refer to previous work from the authors<sup>33</sup> for a complete description of the characterization procedure. Two additional trailing-edge inserts, obtained from the same metal foams but with the addition of 3M EC9323 epoxy adhesive at the symmetry plane, are tested to investigate the effect of the hydrodynamic interaction between the two sides of the airfoil without altering their roughness. For the sake of brevity, the inserts are hereafter referred to as baseline, permeable, and nonpermeable, respectively. Additionally, the exponent of the scaling law  $m$  for far-field acoustic pressure with free-stream velocity  $\overline{p^2} \propto U_\infty^m$ , reported in previous studies for fully or partially porous airfoils manufactured with metal foams with similar properties, is also presented in Table I. It is observed that  $m$  decreases with increasing  $R$  for airfoil trailing edges built with *Alantum* metal foam. Yet, results for different types of metal foam are not in line with this finding: the *Recemat* foam yields the highest exponent ( $m = 7$ ) despite having higher

resistivity than the *Alantum*  $d_c = 800$   $\mu\text{m}$  metal foam. Similarly, the *M-Pore* Al foam, with the lowest resistivity, produces an exponent comparable to those of *Alantum* foams with  $R$  one order of magnitude higher. As a final remark, in Ref. 21, it is reported that far-field acoustic pressure measurements on trailing edges with high resistivity [ $R \in [65 \times 10^3, 278 \times 10^3]$  (N s/m<sup>4</sup>)] foams produce  $m = 5$  when the high-frequency excess noise contribution is excluded; a similar analysis of data published in Ref. 28 was performed by the authors, but similar  $m$  values to those already reported in Table I were found.

## B. Microphone array and acoustic data processing

Acoustic data are recorded with a phased microphone array composed of 64 G.R.A.S. 40PH free-field microphones. A picture of the microphone array placed in the anechoic chamber is shown in Fig. 3. The microphones, with a frequency response precision of  $\pm 1$  dB within 10 Hz–20 kHz, allow for a maximum output of 135 dB (with reference pressure 20  $\mu\text{Pa}$ ).

The microphone distribution, shown in Fig. 4, is optimized to measure frequencies up to 10 kHz with minimum main lobe width and side-lobe level.<sup>34</sup> The effective diameter of the antenna is 2 m, and the distance from the antenna plane to the airfoil trailing edge is 1.48 m. The planar array is parallel to the streamwise-spanwise  $X$ - $Z$  plane. The center of the array is aligned with the center of the airfoil trailing edge.

Far-field noise data are recorded for 60 s at a sampling frequency of 50 kHz. The cross-spectral matrix of the measured acoustic pressure is computed by averaging sample blocks of the signals in the frequency domain.<sup>35</sup> Blocks contain 8192 samples with 50% overlap, and a Hann windowing function is employed. The frequency resolution is thus 6.1 Hz. The main diagonal of the cross-spectral matrix is removed to minimize the effect of incoherent noise measured by each microphone.<sup>36</sup> The refraction of sound waves within the shear layer of the jet is corrected using the method proposed by Sijtsma.<sup>37</sup> Beamforming is applied on a grid ranging between  $-2 < X/c < 2$  and  $-2 < Z/c < 2$  with a spacing of 0.1 cm in both directions.

Conventional frequency domain beamforming<sup>38</sup> retrieves acoustic source maps in one-third octave bands. The acoustic spectra are computed integrating source maps<sup>37</sup> in the range  $-0.27 < Z/c < 0.27$  and  $-0.44 < X/c < 0.41$ ; this technique allows isolating broadband trailing-edge noise from other undesired acoustic sources. The chosen integration area includes all the relevant noise sources generated by the inserts. To achieve a satisfactory signal-to-noise ratio, the measured frequency range includes one-third octave bands with

**TABLE I.** Characteristics of metal foams used in the present experiment or reported in previous studies.<sup>20,28</sup>

Name	$d_c$ ( $\mu\text{m}$ )	$\sigma$ (-)	$K$ ( $\text{m}^2$ )	$R$ (N s/m <sup>4</sup> )	$C$ (m <sup>-1</sup> )	$m$
Alantum	450	0.893	$6 \times 10^{-10}$	29 850	9758	5.5 <sup>28</sup>
Alantum	580	0.905	$1.8 \times 10^{-9}$	10 078	3052	6.1 <sup>28</sup>
Alantum	800	0.917	$2.7 \times 10^{-9}$	6 728	2613	6.4 <sup>28</sup>
Recemat <sup>20</sup>	...	>0.95	...	8 200	...	7
M-Pore Al <sup>20</sup>	...	0.9	...	1 000	...	5.8



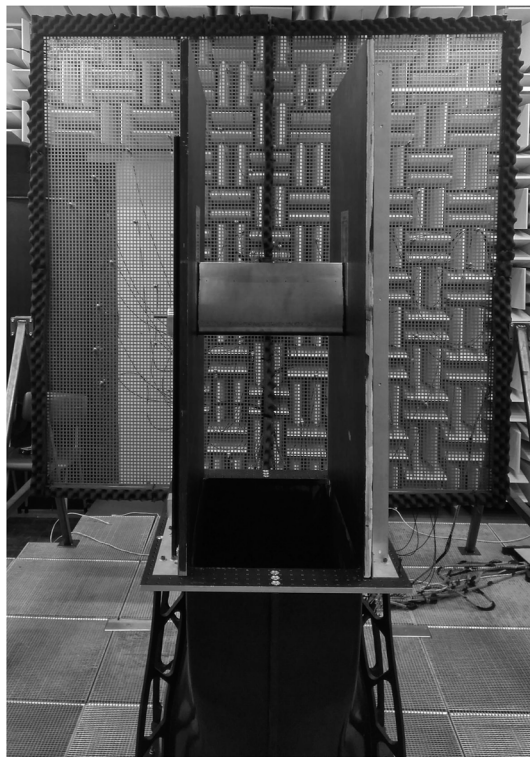


**FIG. 3.** Picture with the test section and model in baseline configuration in front and microphone array behind.

the center frequency ranging from 0.5 to 2.5 kHz. Computed spectra match sound levels measured by the center microphone up to 1 kHz. Rayleigh's criterion<sup>39</sup> sets the minimum distance between two distinguishable noise sources at 12 cm for the highest measured

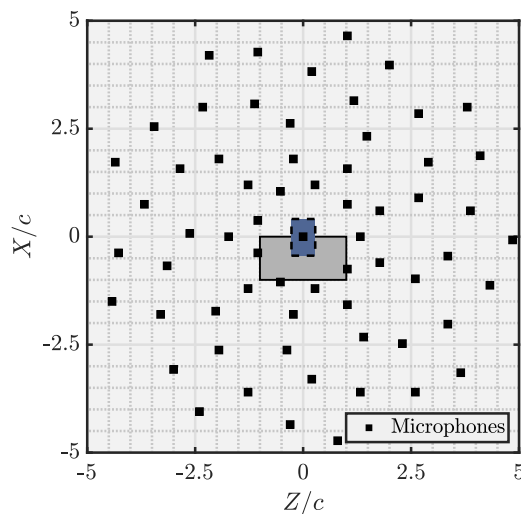


**FIG. 4.** Sketch with microphone distribution. The airfoil is depicted as a gray rectangle, and the integration area location is marked by the blue dashed area.

frequency; the grid spacing is thus 120 times smaller than the maximum resolution of the array, allowing for an accurate localization of the noise sources within the maps. Similar acoustic data processing is successfully employed in previous trailing-edge noise studies.<sup>40</sup> With the current experimental setup and data postprocessing, the uncertainty on the reported noise levels is estimated to be  $\pm 1$  dB, based on a previously reported comparison with synthetic data.<sup>41</sup>

### C. Particle image velocimetry setup

Two-dimensional PIV experiments are conducted to synchronously measure velocity fields at the midspan plane at both sides of the airfoil. The experimental setup is depicted in Fig. 5(a). The flow is seeded with tracers by a SAFEX Twin-Fog Double Power generator using a glycol-based solution with a median droplet diameter of 1  $\mu\text{m}$ .<sup>42</sup> Illumination is provided by a Continuum MESA PIV

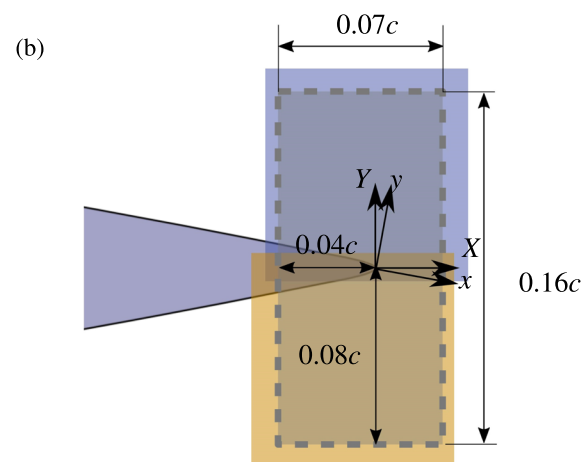
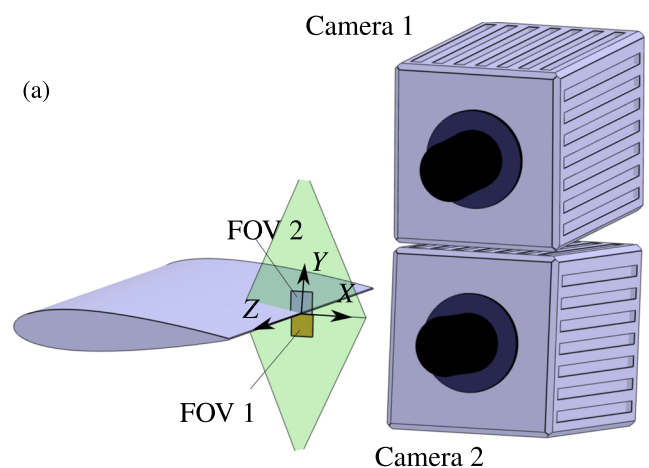


**FIG. 5.** (a) Sketch of the PIV setup. (b) Detail of the FOV and coordinate system. The original FOV of the cameras are represented by the blue and orange areas. The final FOV, obtained after joining and cropping them, is marked with the gray dashed shadowed area. Note that in the experiment, the airfoil was positioned vertically instead of horizontally.

532-120-M Nd:YAG system; each pulse, with a maximum output of 18 mJ, is emitted at a wavelength of 532 nm. To illuminate simultaneously both sides of the airfoil, 2 coplanar laser sheets (with thickness equal to 1 mm) are obtained from the same light source with a combination of beam-splitter, mirrors, and convex/concave lenses.

Particle images are acquired with two *Photron* Fastcam SA-1 CMOS cameras ( $1024 \times 1024$  pixel<sup>2</sup>, 12 bit, pixel size 20  $\mu\text{m}$ ), placed at 25 cm from the measurement plane. The cameras are equipped with *Nikon*  $f' = 200$  mm macrolenses set to aperture  $f_\# = 4$ . With the current setup, the particle-image diameter<sup>43</sup> is 5  $\mu\text{m}$  (0.25 pixel). To minimize peak-locking,<sup>44</sup> an offset between the focusing plane and the laser sheet is set, hence achieving an image of the particle larger than 2 pixels.<sup>45</sup> The illumination and image acquisition are triggered synchronously using a *LaVision* high speed controller. Time-resolved data are acquired at a sampling frequency of 20 kHz cropping the sensor of the camera to  $512 \times 512$  pixels. The acquisition time, equal to 1.1 s, is limited by the internal memory of the cameras. For the lowest frequency studied in the flow-field analysis (447 Hz, in agreement with the acoustic analysis), 488 cycles are thus acquired. Each camera records a field of view (FOV) of  $0.1c \times 0.1c$  ( $20 \times 20$  mm<sup>2</sup>) with a digital resolution of approximately 25 pixels mm<sup>-1</sup>. After calibration, the single FOVs are combined yielding to a total FOV of  $0.16c \times 0.07c$  ( $32 \times 14$  mm<sup>2</sup>), as shown in Fig. 5(b). The final measured area ranges between  $-0.04 \leq X/c \leq 0.03$  and  $-0.08 \leq Y/c \leq 0.08$ . The  $x$ - $y$ - $z$  coordinate system [Fig. 5(b)], used for boundary layer flow analysis, is rotated with respect to the  $X$ - $Y$ - $Z$  coordinate system so that the  $x$  and  $y$  directions are, respectively, parallel and normal to the surface of the trailing-edge insert independently of the side of the airfoil. Both coordinate systems have the same origin.

Particle images are processed using *LaVision* DaVis 8.4. A multipass cross correlation algorithm<sup>46</sup> with window deformation<sup>47,48</sup> is applied to the sequence of images resulting in an ensemble of 21 828 vector fields. The final interrogation window size is  $24 \times 24$  pixel<sup>2</sup> with an overlap factor of 75%, yielding a final spatial resolution of 0.94 mm and a vector spacing of 0.24 mm. The universal outlier detector<sup>49</sup> removes spurious vectors (approximately 0.8% of the total), replacing them with a linear interpolation based on adjacent data. A summary of the system parameters of the PIV setup is presented in Table II.

TABLE II. System parameters of the PIV experiment.

Cameras	<i>Photron</i> Fastcam SA1.1
Acquisition frequency	20 kHz
Acquisition sensor	$512 \times 512$ pixel <sup>2</sup>
Single FOV	$20 \times 20$ mm <sup>2</sup>
Total FOV	$32 \times 14$ mm <sup>2</sup>
Digital resolution	25 pixels mm <sup>-1</sup>
Magnification factor	0.51
Interrogation window	$24 \times 24$ pixel <sup>2</sup>
Overlap factor	75%
Vectors per velocity field	$136 \times 60$
Vector spacing	$0.24 \times 0.24$ mm <sup>2</sup>
Free-stream pixel displacement	20 pixels

Main sources of errors affecting the measurement of kinematic quantities are due to the positioning of the calibration target, cross correlation,<sup>45</sup> particle slip,<sup>50</sup> and the convergence of statistical quantities. In the present study, the uncertainty of the measurement is quantified using the method presented by Wieneke;<sup>51</sup> this method measures the correlation between image pairs, once the second frame is projected back to the first one with the computed particle displacement field. Considering a 95% confidence interval, the analysis yields a higher bound uncertainty on mean quantities of 0.5% of the free-stream velocity and on the root-mean-square (rms) quantities of  $0.03\sqrt{u^2}$  (at  $x/c = 0$ ,  $y/\delta = 0.45$ ).

#### D. Symmetry of the setup and validation of the flow field measurements

The airfoil is set at approximately zero degree angle of attack using a *Wyler* Clinotronic inclinometer. Accounting for the misalignment between the jet and the floor, as well as the accuracy of the inclinometer, the total accuracy of the angle of attack is estimated as  $0.2^\circ$ . To further assess it, static pressure measurements are obtained through 15 differential pressure *Honeywell* TruStability transducers (range:  $-0.6$  to  $0.6$  kPa; accuracy: 3 Pa), which are connected to 30 pressure taps with a diameter of 0.4 mm. The orifices are distributed from 1% to 66% of the chord. The pressure taps are located along a plane slanted  $15^\circ$  and with an offset of 2 cm with respect to the midspan plane of the airfoil [Fig. 2(a)]. This arrangement prevents flow interference between consecutive pressure taps.<sup>54</sup> Pressure measurements are carried out at a sampling rate of 100 Hz for 10 s. The angle of attack is determined by comparing the measured differential static surface pressure  $\Delta C_p = (p_{ss} - p_{ps})/(1/2\rho U_\infty^2)$  distribution against XFOIL results,<sup>55</sup> shown in Fig. 6(a). The measured pressure distribution agrees within uncertainty range (computed using a linear propagation approach<sup>56</sup>) with the one for a model in free-air conditions set at  $0.05^\circ$ ; the angle of attack is, therefore, considered negligible.

The verification of the angle of attack is also performed by comparing boundary layer quantities measured at suction and pressure sides. Specifically, the streamwise variation of boundary layer thickness  $\delta_{99}$  and momentum thickness  $\theta$  is compared in Figs. 6(b) and 6(c). A detailed description of the computation procedure for these quantities is given in the following paragraph. The uncertainty is estimated as  $\pm 0.25$  mm and  $\pm 0.05$  mm for  $\delta$  and  $\theta$ , respectively, in line with León *et al.*<sup>52</sup> Results show agreement within the uncertainty range; hence, the symmetry of the experimental setup is confirmed.

Data measured at the trailing edge ( $X/c = 0$ ) are further compared with previous research. Apart from  $\delta$  and  $\theta$ , displacement thickness  $\delta_*$  and friction velocity  $U_\tau \equiv \sqrt{\tau_w/\rho}$  (where  $\tau_w$  refers to wall shear stress and  $\rho$  refers to the fluid density) values reported from similar experiments<sup>52,53</sup> and XFOIL are also used for comparison (Table III). In this study,  $\delta$  is estimated as the location where the mean wall-parallel velocity is 99% of the edge velocity  $U_e$ . The latter quantity is computed based on the integral of the spanwise vorticity along the wall-normal direction, as proposed in Ref. 57. The comparison shows an overall good agreement for all the boundary layer length scales with the exception of  $\delta_*$  (therefore,  $H$ ). It is found that the  $\delta_*$  values reported by León *et al.*<sup>52</sup> and XFOIL are lower than current data. The disagreement is consistent with the

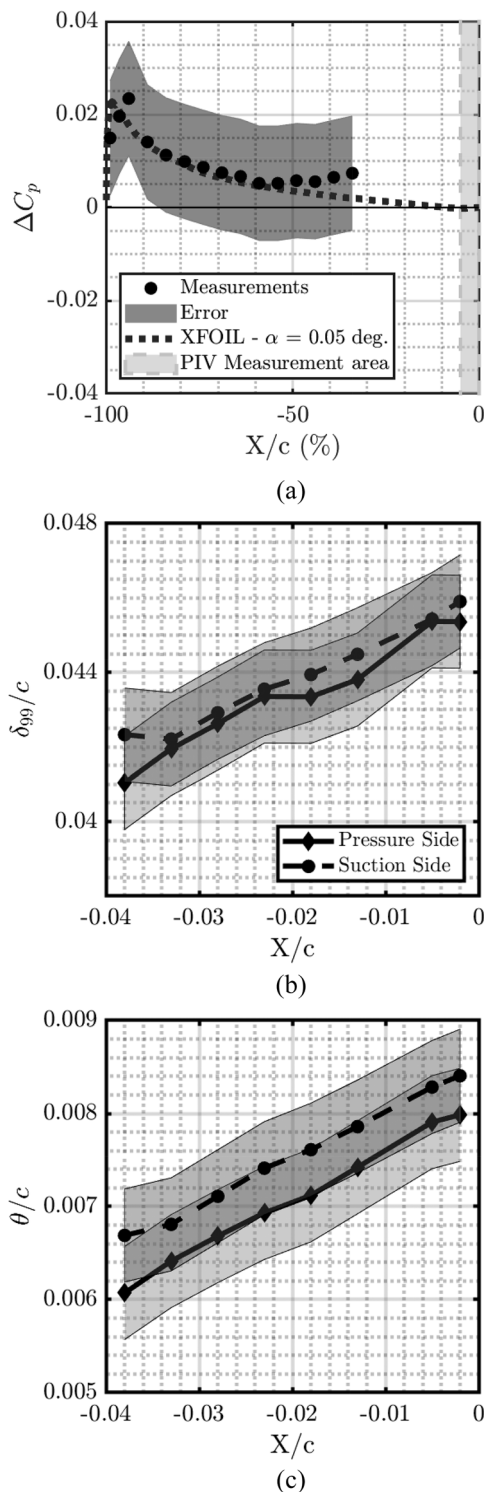


**FIG. 6.** Symmetry of the baseline configuration. (a) Differential static pressure distribution  $\Delta C_p$  along the chord of the model. (b) Boundary layer thickness  $\delta_{99}/c$  measured at suction and pressure sides for the baseline configuration. (c) Momentum thickness  $\theta/c$ .

**TABLE III.** Comparison of boundary layer thickness  $\delta$  (in mm), displacement thickness (in mm)  $\delta_*$  (in mm), momentum thickness  $\theta$  (in mm), shape factor  $H$ , and friction velocity  $U_\tau$  (in m/s) values measured at both sides of the solid trailing edge ( $X/c = 0$ ) with the values presented in previous studies and XFOIL. SS and PS stand for the values measured at suction and pressure sides of the airfoil in the present experiment.

Investigation	$\delta$	$\delta_*$	$\theta$	$H$	$U_\tau$	$Re_c$	$Re_\theta$
León <i>et al.</i> <sup>52</sup>	9.4	2.1	1.3	1.6	...	263 000	1700
Avallone <i>et al.</i> <sup>53</sup>	9.5	3.3	1.5	2.2	...	280 000	2100
XFOIL	...	2.3	1.2	1.9	0.41	263 000	1580
Present (SS)	9.2	3.5	1.5	2.3	0.42	263 000	1980
Present (PS)	9.1	3.4	1.5	2.3	0.41	263 000	1980

difference in boundary layer turbulator size.  $U_\tau$  values are calculated following Clauser<sup>58</sup> through the fit of  $U$  with the logarithmic law<sup>59</sup> using universal constants  $\kappa$  and  $C$  equal to 0.41 and 5.1, respectively. Data above  $y/\delta = 0.15$  match the aforementioned law; therefore, only values within this range are reported in the remaining of this manuscript. Agreement between the measured  $U_\tau$  and that of XFOIL is also satisfactory.

Finally, the mean streamwise velocity  $U/U_\infty$  profile at the wake location  $X/c = 0.02$ , shown in Fig. 7 for all the test cases, is analyzed. Profiles are symmetric with respect to  $Y/c = 0$  independently of the insert; hence, the employment of permeable inserts at the trailing edge does not alter the symmetry of the mean flow field. Interestingly, an increased velocity deficit (up to  $0.03U_\infty$  with respect to the baseline case) is observed for the metal foam inserts with the largest pore size independently of the permeability. This finding is in line with previous experiments, which attributed this phenomenon to a higher surface drag caused by roughness.<sup>60</sup> Consequently, the drag coefficient  $C_D$ , which is computed based on the wake velocity deficit<sup>61</sup> as

$$C_D = \frac{2}{c} \int \frac{U}{U_\infty} \left(1 - \frac{U}{U_\infty}\right) dY, \quad (1)$$

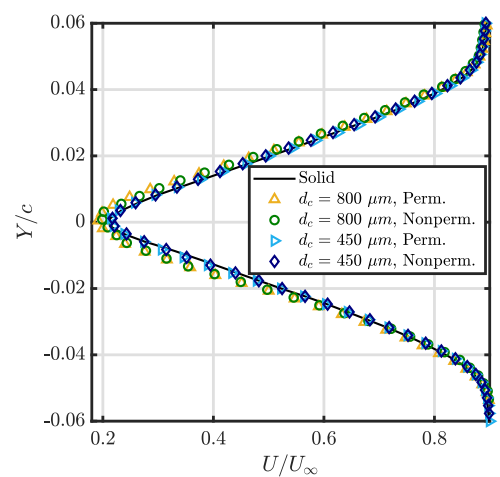


**FIG. 7.** Normalized mean velocity profile  $U/U_\infty$  at the wake ( $X/c = 0.02$ ) for the baseline case as well as the metal foam inserts.



**TABLE IV.** Comparison between drag coefficient  $C_D$  values computed for different inserts.

Case	$C_D$
Solid	0.0273
$d_c = 450 \mu\text{m}$ , permeable	0.0272
$d_c = 450 \mu\text{m}$ , nonpermeable	0.0274
$d_c = 800 \mu\text{m}$ , permeable	0.0280
$d_c = 800 \mu\text{m}$ , nonpermeable	0.0280

is approximately 3% higher for the metal foam inserts with  $d_c = 800 \mu\text{m}$  (with length equal to 20% of the chord) than for the solid case, as reported in Table IV.

For additional description of the boundary layers, the reader is referred to a preliminary analysis available in Ref. 28.

### E. Correlation maps computation methodology

As explained in Sec. I, the main scope of this investigation is to prove that the employment of permeable materials mitigates the pressure jump at the trailing edge, hence resulting in decreased noise scattering with respect to a fully solid edge. Due to the complexity related to the nonintrusive characterization of flow within porous media,<sup>62</sup> an alternative approach is followed; the analysis is focused on revealing correlation between turbulent fluctuations at both sides of the airfoil. Such a finding would imply the existence of flow connection through permeable media. With this aim, two-point two-dimensional spatial correlations, generally employed to characterize the spatial organization of turbulent structures,<sup>63</sup> are extensively used. Specifically, wall-normal velocity fluctuations are investigated due to their link to hydrodynamic wall-pressure fluctuations,<sup>64–66</sup> widely used as the source term in analytical models for solid trailing-edge noise.<sup>26,67</sup>

The two-point spatial cross correlation function of the wall-normal velocity fluctuations  $R_{vv}(\mathbf{x}, \xi)$  is conventionally defined as<sup>68</sup>

$$R_{vv}(\mathbf{x}, \xi) = \frac{\overline{v(\mathbf{x})v(\mathbf{x} + \xi)}}{\sqrt{\overline{v(\mathbf{x})^2}}\sqrt{\overline{v(\mathbf{x} + \xi)^2}}}, \quad (2)$$

where  $\mathbf{x}$  is the reference point and  $\xi$  is the separation vector. However, the normalization of the covariance employed in Eq. (2) provokes an artificial increase in  $R_{vv}(\mathbf{x}, \xi)$  at locations where the rms velocity has low values, i.e., close to the outer boundary layer edge, which complicates the interpretation of the results.<sup>69</sup> To avoid this issue, in the present analysis, the spatial cross correlation is computed as

$$R_{vv}^*(\mathbf{x}, \xi) = R_{vv}(\mathbf{x}, \xi) \sqrt{\frac{\overline{v(\mathbf{x} + \xi)^2}}{\overline{v(\mathbf{x})^2}}} = \frac{\overline{v(\mathbf{x})v(\mathbf{x} + \xi)}}{\overline{v(\mathbf{x})^2}}. \quad (3)$$

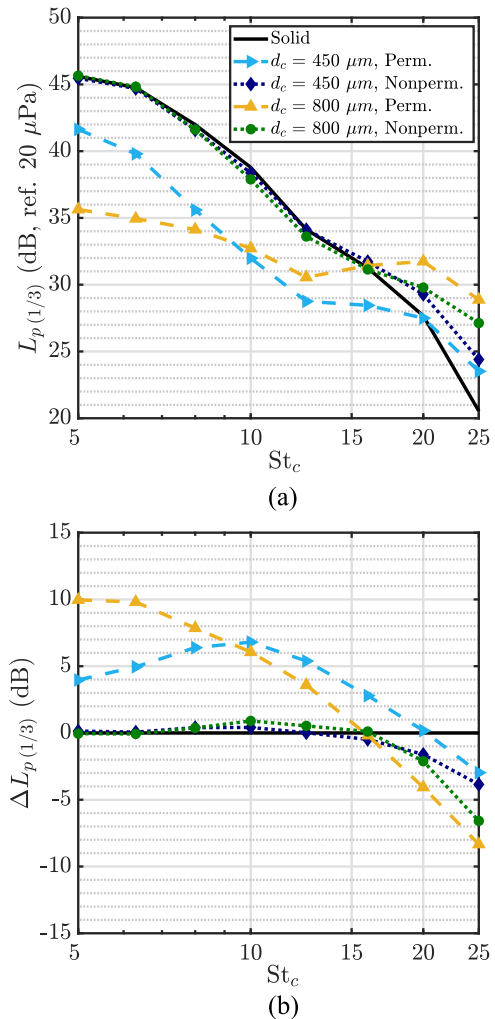
In this way, statistical quantities measured at  $\mathbf{x} + \xi$  are removed from the denominator of Eq. (2). This definition is usually employed in trailing-edge noise research<sup>70,71</sup> due to its accuracy. The term “correlation” is hereafter employed to refer to the quantity defined in Eq. (3), calculated over the 21 828 flow-field snapshots, and computed by selecting a reference position and varying  $\xi$  within the

measured FOV. For a better visualization, correlation maps computed with reference points at the lower side are flipped with respect to  $Y/c = 0$  and averaged with those obtained with reference points at mirrored locations.<sup>72</sup> Small, isolated low-correlation spots are also removed from the maps for the sake of clarity.

### III. FAR-FIELD NOISE

Far-field acoustic scattering [Fig. 8(a)] is presented in terms of sound pressure level integrated in one-third octave bands  $L_{p(1/3)} = 10 \log_{10}(\overline{p^2}/p_{\text{ref}}^2)$ , where  $p_{\text{ref}} = 20 \mu\text{Pa}$  is the reference pressure, as a function of the Strouhal number based on the chord and the free-stream velocity  $St_c = f_c c/U_\infty$ . For the sake of clarity,  $L_p$  values relative to the baseline case  $\Delta L_p = L_p^{\text{solid}} - L_p^{\text{metal foam}}$  are also shown in Fig. 8(b).

In the spectra shown in Figs. 8(a) and 8(b), two different regions can be detected. In the low frequency range, fully permeable

**FIG. 8.** Far-field noise spectra. (a) Absolute  $L_{p(1/3)}$  values. (b) Relative  $L_{p(1/3)}$  values with respect to the baseline case.

trailing edges show noise reduction with respect to the solid trailing edge while avoiding flow communication results in similar noise scattering as for the solid edge. Hence, for the present inserts, low-frequency noise reduction is solely caused by the permeability; this result can be related to the presence of cross-flow that will be further investigated in Sec. IV. At higher frequencies, noise increase with respect to the baseline configuration is measured. These two regions are separated by a cross-over  $St_c^* = 16$  ( $f_c = 1.6$  kHz) for the two non-permeable inserts and the permeable  $d_c = 800$   $\mu\text{m}$  foam insert, while for the permeable insert with  $d_c = 450$   $\mu\text{m}$ , the  $St_c^*$  is equal to 20 ( $f_c = 2$  kHz).

As expected,<sup>21</sup> below  $St_c^*$ , permeable materials with increasing permeability produce higher noise attenuation levels. More in detail, up to 7 (at  $St_c = 10$ ) and 10 dB (at  $St_c = 5$ ) noise abatement are measured for permeable inserts manufactured with  $d_c = 450$   $\mu\text{m}$  and  $d_c = 800$   $\mu\text{m}$  foam, respectively. Interestingly, below  $St_c = 12.5$ , the absolute noise spectra corresponding to the least permeable foam and baseline cases share a similar slope. Yet, for the most permeable metal foam, there is a remarkable change in the slope with respect to the baseline configuration. These two aspects will be linked (see Sec. V) to fundamental changes in the noise generation process caused by the employment of metal foams with different permeability.

Above  $St_c^*$ , maximum excess noise is measured at  $St_c = 25$  for all the porous inserts. This feature has been already reported in previous experimental work involving porous trailing edges.<sup>22</sup> Due to its high-frequency nature and the fact that higher noise levels are reported for materials with larger pore size, it was attributed to roughness noise.<sup>73</sup> The present results confirm that this feature is indeed mostly due to the rough characteristics of the metal foam surface. Yet, the fact that permeable and nonpermeable inserts manufactured with the same material generate different excess noise levels (up to 2 dB) suggests that additional aeroacoustic phenomena occur due to the permeability. This point will be also addressed below.

#### IV. CORRELATION OF VELOCITY FLUCTUATIONS

In Sec. III, it was shown that only permeable inserts reduce noise with respect to the solid trailing edge. This result suggests that

the open connection between the two sides of the airfoil through the metal foam significantly alters the mechanism of noise generation at the edge, eventually resulting in decreased noise scattering. In this section, correlation maps, as defined in Sec. II E, are employed to assess the presence of cross-flow in the cases where noise reduction with respect to the baseline configuration is reported.

First, maps of the cross correlation function as defined in Eq. (3) are plotted in Figs. 9(a)–9(e) for the five test cases. The maps depict only zones of positive correlation, while zones of negligible or negative correlation ( $R_{vv}^* < 0.02$ ) are masked. The reference point, located at  $\mathbf{x}/c = (X/c, Y/c) = (-0.02, 0.013)$ , is marked by a black square. To link the presence of flow communication to the measured noise abatement, data are bandpass filtered within  $St_c \in [4, 16]$  for inserts manufactured with  $d_c = 800$   $\mu\text{m}$  foam insert and the nonpermeable  $d_c = 450$   $\mu\text{m}$  foam insert, and  $St_c \in [4, 20]$  for the permeable  $d_c = 450$   $\mu\text{m}$  foam insert. To compare, velocity fluctuations measured for the solid case are also filtered out using the latter nondimensional frequency range.

As shown in Figs. 9(a)–9(e), the energy transfer from large coherent motions within the outer boundary layer to the near-wall region<sup>74,75</sup> creates correlation zones surrounding the reference point and elongated toward the wall-normal direction independently of the test case. For the solid and nonpermeable metal foam cases [Figs. 9(a), 9(c), and 9(e)], regions of high correlation only appear around the reference point or within the wake; turbulent motions at upper and lower sides are not correlated, i.e., cross-flow is absent due to the presence of a solid boundary in between both sides. For the nonpermeable  $d_c = 800$   $\mu\text{m}$  foam insert [Fig. 9(e)], an increase in the streamwise extent of the correlation zone around the reference point is reported. Irregular rough surfaces usually introduce a certain degree of disorganization in the turbulent flow, particularly in the flow direction, hence decreasing the associated length scales.<sup>76</sup> Ali *et al.*<sup>77</sup> reported the appearance of recirculation flow inside blunt trailing-edge permeable extensions; the streamwise enlargement of the correlation zone might be, therefore, related to this phenomenon. The lower permeability of the  $d_c = 450$   $\mu\text{m}$  foam insert [Figs. 9(b) and 9(c)] might weaken or even fully prevent this flow feature, supporting the absence of significant differences between correlation zones surrounding the reference point for permeable and nonpermeable configurations. Contrary to the baseline and

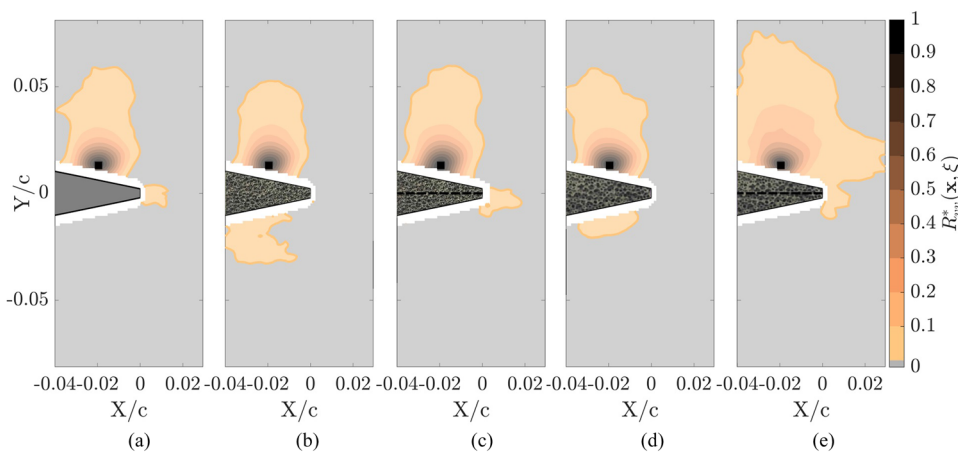


**FIG. 9.** Low-frequency wall-normal velocity fluctuation correlation maps with reference point at  $\mathbf{x}/c = (X/c, Y/c) = (-0.02, 0.013)$  ( $y/\delta_{\text{ref}} = 0.15$ ). (a) Solid. (b) Permeable  $d_c = 450$   $\mu\text{m}$  foam insert. (c) Nonpermeable  $d_c = 450$   $\mu\text{m}$  foam insert. (d) Permeable  $d_c = 800$   $\mu\text{m}$  foam insert. (e) Nonpermeable  $d_c = 800$   $\mu\text{m}$  foam insert.

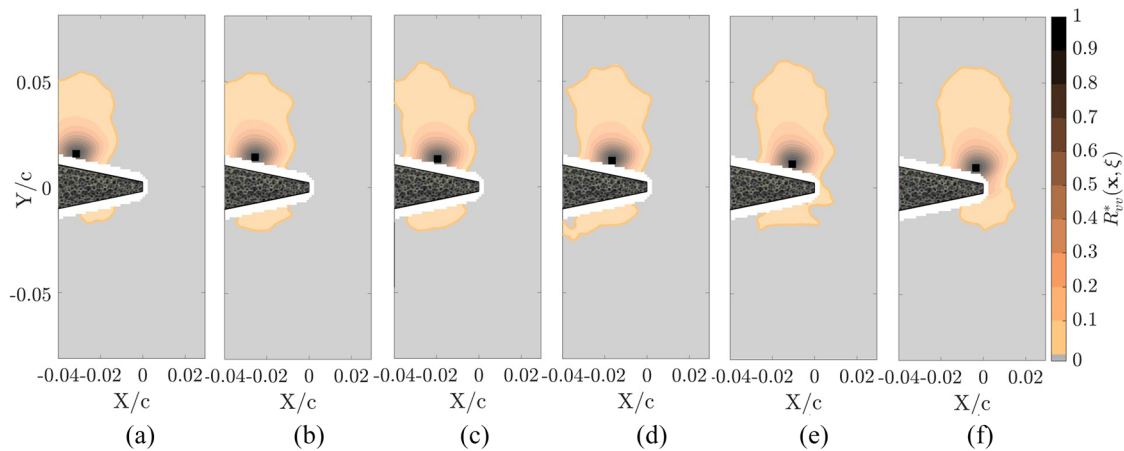


**FIG. 10.** Low-frequency wall-normal velocity fluctuations correlation maps for the permeable  $d_c = 800 \mu\text{m}$  foam insert with reference point at different streamwise locations. (a)  $X/c = -0.032$ ,  $Y/c = 0.016$ ; (b)  $X/c = -0.026$ ,  $Y/c = 0.014$ ; (c)  $X/c = -0.020$ ,  $Y/c = 0.013$ ; (d)  $X/c = -0.016$ ,  $Y/c = 0.012$ ; (e)  $X/c = -0.011$ ,  $Y/c = 0.011$ ; (f)  $X/c = -0.004$ ,  $Y/c = 0.01$ .

nonpermeable inserts, for permeable inserts, a near-wall low-correlation ( $0.02 < R_{vw}^* < 0.1$ ) region appears at the lower side, regardless of the type of foam [Figs. 9(b) and 9(d)]; the presence of unsteady flow connection across the airfoil is thus confirmed.

Before assessing the implications of this finding on noise generation, the properties of correlation regions found at both sides of the permeable trailing-edge mock-ups are addressed. First, their appearance within the measured streamwise extent of permeable treatments is analyzed. In Figs. 10(a)–10(f), it is shown that the appearance of correlation zones at the lower side of the  $d_c = 800 \mu\text{m}$  insert is independent of the streamwise position of the reference point; this result evidences the presence of effective flow communication through the entire measured extension. The smaller

correlation zone found when the reference point is moved upstream can be attributed to increased viscous and inertial losses due to the larger thickness of the insert.<sup>78</sup> It is also interesting to note that for the most upstream reference point location [Fig. 10(a)], the correlation zone is located slightly downstream the reference point, indicating that flow communication through the foam occurs following preferred flow directions. Such a finding might be related to the presence of a pressure gradient between the two sides of the airfoil. Similar conclusions are also drawn for the least permeable foam ( $d_c = 450 \mu\text{m}$ ) insert, shown in Figs. 11(a)–11(f).

The extension of the lower-side correlation zone is also strongly influenced by the distance between the reference point and the wall. In Figs. 12(a)–12(d), correlation maps for reference points ranging

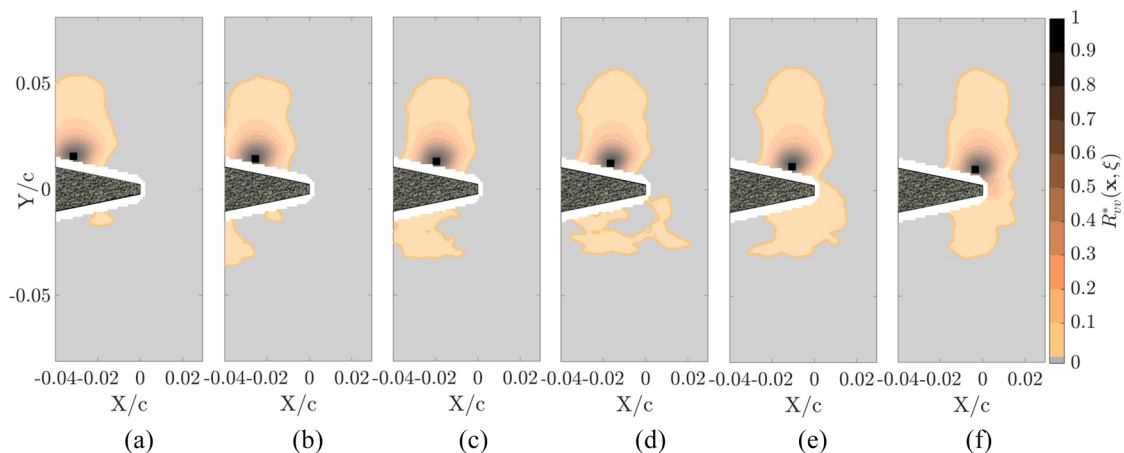


**FIG. 11.** Low-frequency wall-normal velocity fluctuations correlation maps for the permeable  $d_c = 450 \mu\text{m}$  foam insert with reference point at different streamwise locations. Locations are specified in the caption of Fig. 10.

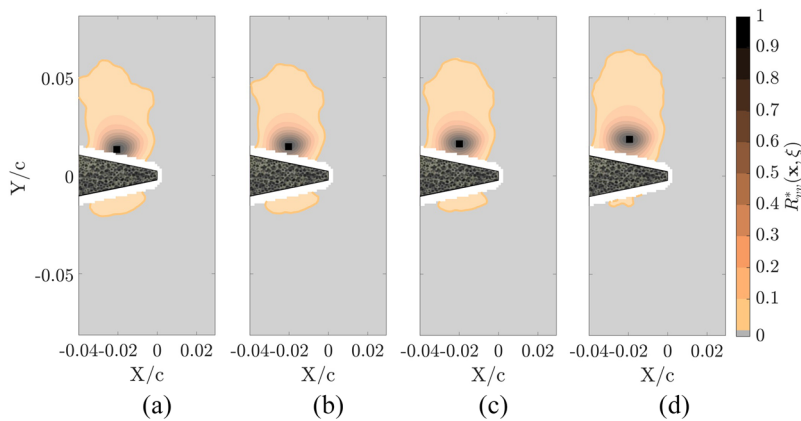


**FIG. 12.** Low-frequency wall-normal velocity fluctuations correlation maps for the permeable  $d_c = 800 \mu\text{m}$  foam insert with reference point at different wall-normal locations. (a)  $y/\delta_{\text{ref}} = 0.15$ ; (b)  $y/\delta_{\text{ref}} = 0.18$ ; (c)  $y/\delta_{\text{ref}} = 0.21$ ; (d)  $y/\delta_{\text{ref}} = 0.25$ .

from  $y/\delta_{\text{ref}} = 0.15$  to  $y/\delta_{\text{ref}} = 0.25$  (where  $\delta_{\text{ref}}$  is the boundary layer thickness at the trailing edge for the baseline case) at  $X/c = -0.02$  are shown for the permeable  $d_c = 800 \mu\text{m}$  foam insert. It is found that correlated velocity fluctuations at the other side appear until a wall-normal distance of the reference point equal to 25% of the boundary layer; hence, only near-wall turbulent motions are influenced by the absence of a solid boundary in between the upper and lower sides of the airfoil. Although this analysis is not shown for the permeable  $d_c = 450 \mu\text{m}$  foam insert for the sake of brevity, similar results are found.

As explained above, the appearance of near-wall correlated flow regions implies the presence of cross-flow linking the suction and pressure sides of the airfoil within the permeable medium. This remarkable flow feature has direct implications on the edge noise generation of permeable lifting bodies: as reported by Delfs *et al.*,<sup>23</sup> flow communication through the permeable inserts partially phases wall-pressure waves at both sides of the airfoil, hence decreasing the unsteady pressure mismatch at the edge. This process eventually results in far-field noise abatement within the frequency range where turbulent motions are phased, in agreement with the results presented in Sec. III. As also

pointed out Ref. 24, permeable materials might also trigger noise scattering from different streamwise locations, thus allowing constructive/destructive interference between noise sources arising along the insert. This point will be addressed in Sec. V, where the presence of different noise sources within the inserts for the five test cases will be assessed.

To underline the link between cross-flow and noise abatement, the cross correlation analysis is also applied to datasets bandpass filtered using the frequency range where excess noise was previously reported. Specifically, wall-normal velocity fluctuations within  $\text{St}_c \in [16, 25]$  for inserts manufactured with  $d_c = 800 \mu\text{m}$  and the nonpermeable  $d_c = 450 \mu\text{m}$  foam insert, and  $\text{St}_c \in [20, 25]$  for the permeable  $d_c = 450 \mu\text{m}$  foam insert are considered. Correlation maps computed on these datasets are shown in Figs. 13(a)–13(e); results show no evidence of correlation regions on the complementary side of the airfoil, in line with the results described in Sec. III. Further assessment is given in Figs. 14(a)–14(f), where correlation maps obtained by varying the streamwise position of the reference point are presented for the most permeable foam; it can be observed that no correlation at the lower side is found even when the point is placed above the trailing edge, where the thickness of the metal foam is minimal.

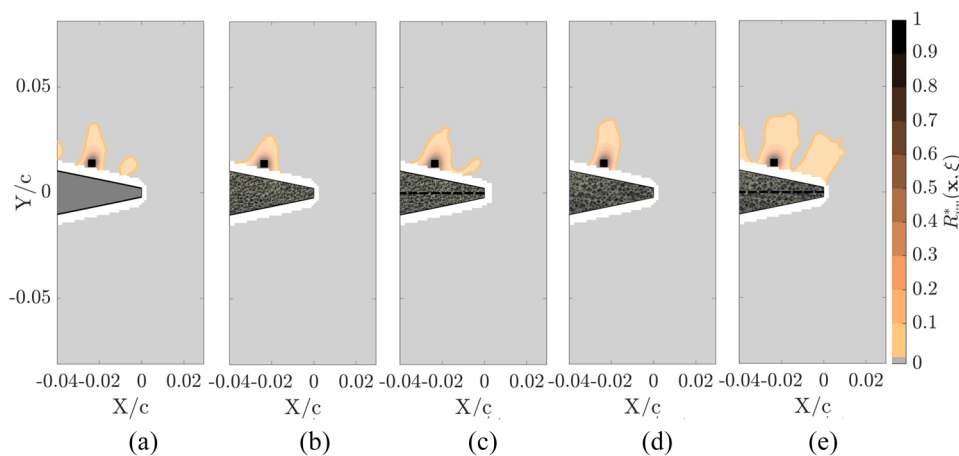


**FIG. 13.** High-frequency wall-normal velocity fluctuation correlation maps with reference point at  $\mathbf{x}/c = (X/c, Y/c) = (-0.02, 0.013)$  ( $y/\delta_{\text{ref}} = 0.15$ ). (a) Solid. (b) Permeable  $d_c = 450 \mu\text{m}$  foam insert. (c) Nonpermeable  $d_c = 450 \mu\text{m}$  foam insert. (d) Permeable  $d_c = 800 \mu\text{m}$  foam insert. (e) Nonpermeable  $d_c = 800 \mu\text{m}$  foam insert.

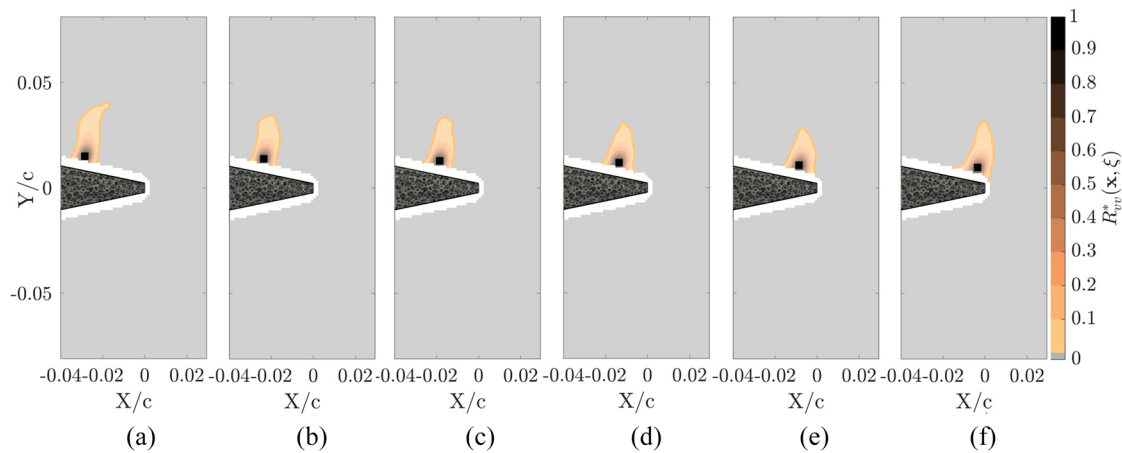


**FIG. 14.** High-frequency wall-normal velocity fluctuation correlation maps for the permeable  $d_c = 800 \mu\text{m}$  foam insert with reference point at different streamwise locations. (a)  $X/c = -0.032$ ,  $Y/c = 0.016$ ; (b)  $X/c = -0.026$ ,  $Y/c = 0.014$ ; (c)  $X/c = -0.020$ ,  $Y/c = 0.013$ ; (d)  $X/c = -0.016$ ,  $Y/c = 0.012$ ; (e)  $X/c = -0.011$ ,  $Y/c = 0.011$ ; (f)  $X/c = -0.004$ ,  $Y/c = 0.01$ .

## V. ACOUSTIC SOURCE MAPS

Noise source maps are hereafter analyzed to verify any displacement of the predominant sound source detected by the microphone antenna. The current analysis is limited by the resolution of the array;<sup>79</sup> yet, it might allow us to qualitatively identify different mechanisms involved in the process of sound generation for the test cases discussed.

Figures 15(a)–15(e) show acoustic source maps for  $St_c = 10$  ( $f_c = 10 \text{ kHz}$ ) for the five measured inserts. At this  $St_c$ , noise abatement with respect to the baseline configuration was reported only for permeable inserts in Sec. III. In the maps, the location of maximum noise intensity within  $-1 < Z/c < 1$  is indicated by a red dashed-dotted line. For the solid case [Fig. 15(a)], the red line is aligned with the trailing edge, as expected from the distributed line

source nature of broadband trailing-edge noise.<sup>80</sup> Similarly, for the nonpermeable metal foam inserts [Figs. 15(c) and 15(e)], noise is mainly scattered from the trailing edge and the intensity of the sound source is similar to the baseline case. Hence, within this frequency range, the location of the noise source is not altered by the presence of rougher surfaces, in agreement with the results presented in Sec. III. For permeable inserts [Figs. 15(b) and 15(d)], in addition to the reduction of the sound power caused by the mitigation of the pressure jump, it is also found that the maximum sound emission is located more upstream. The employment of permeable materials thus promotes distributed noise scattering from different streamwise locations, in agreement with analytical models<sup>24</sup> and numerical simulations.<sup>23</sup> This aspect will be further investigated in the following.

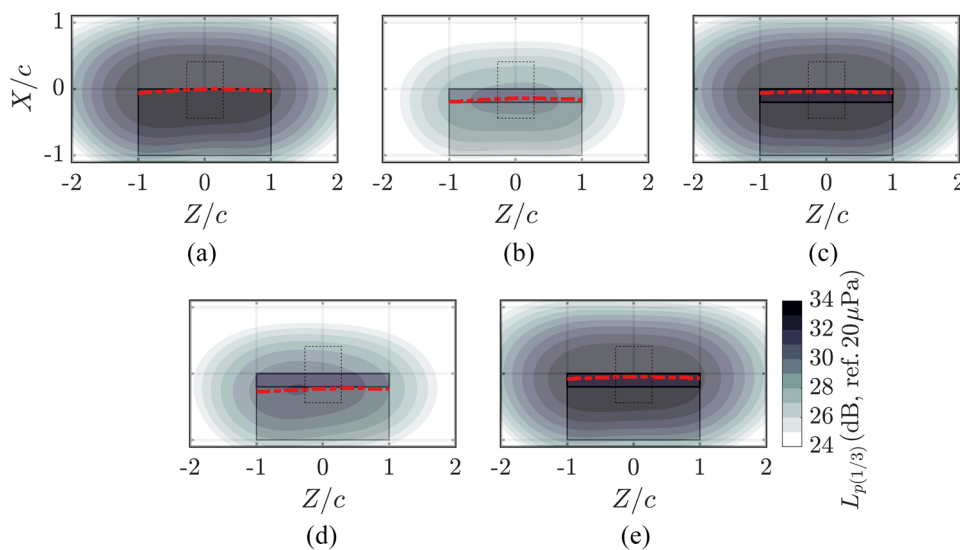


**FIG. 15.** Source maps for the one-third octave band with  $f_c = 1000 \text{ Hz}$  ( $St_c = 10$ ) for the measured test cases. (a) Solid. (b) Permeable  $d_c = 450 \mu\text{m}$  foam insert. (c) Nonpermeable  $d_c = 450 \mu\text{m}$  foam insert. (d) Permeable  $d_c = 800 \mu\text{m}$  foam insert. (e) Nonpermeable  $d_c = 800 \mu\text{m}$  foam insert. The airfoil is represented as a gray rectangle. Metal foam inserts are depicted with dark gray rectangles. Dashed area represents the region where the source power integration technique is applied. Red dashed-dotted line marks streamwise  $L_{p(1/3)}$  maxima within  $-1 < Z/c < 1$ .



Acoustic source maps for  $St_c = 20$  ( $f_c = 2$  kHz) are presented in Figs. 16(a)–16(e). Within this nondimensional frequency band, noise increase due to roughness was found in Sec. III. For the baseline case, similar to the results obtained for lower frequencies, the dominant noise source is aligned with the trailing edge [Fig. 16(a)]. Conversely, for the porous configurations [Figs. 16(b)–16(e)], the maximum noise emission lies upstream the edge independently of the permeability. The noise source shift can be caused by the distributed nature of roughness noise and confirms that this mechanism is mainly responsible for the excess noise reported in Sec. III. In Figs. 8(a) and 8(b), it was observed that the permeable  $d_c = 800$   $\mu\text{m}$  metal foam mock-up produced higher excess noise levels than the nonpermeable version, whereas the  $d_c = 450$   $\mu\text{m}$  inserts behaved oppositely. In agreement with Kisil and Ayton,<sup>24</sup> this interesting result points out that apart from the roughness noise contribution, other noise generation mechanisms such as interference between sources distributed streamwisely along the insert or unsteady volume flow injection/ejection<sup>81</sup> due to permeability might also be present.

The streamwise position of the maximum noise emission within the source maps as a function of  $St_c$  is analyzed in the following. Absolute streamwise coordinates normalized by the chord  $X_{L_{p(1/3)}^{\max}}/c$  are presented in Fig. 17(a). Note that as expected, at low  $St_c$ , the absolute location of the main noise emission is shifted due to the low resolution of the array, and an accurate source localization is only obtained above  $St_c = 10$  ( $f_c = 1$  kHz). However, it is considered that the shift affects every reported test case similarly; as a consequence, the analysis of the main source position relative to the solid edge  $\Delta X_{L_{p(1/3)}^{\max}}/c = X_{L_{p(1/3)}^{\max}}^{\text{solid}}/c - X_{L_{p(1/3)}^{\max}}^{\text{metal foam}}/c$ , reported in Fig. 17(b), is expected to yield valuable insights on the nature of the sound generation process present in metal foam inserts.

For the permeable  $d_c = 800$   $\mu\text{m}$  foam insert, the main noise source is upstream the trailing edge; specifically, for the entire investigated frequency range, it is located approximately 4 cm

( $X/c = -0.2$ ) upstream the position of the trailing edge (as retrieved for the solid case), lying near the solid-permeable junction position. In agreement with analytical<sup>24</sup> and numerical solutions,<sup>23</sup> this finding suggests that cross-flow decreases the pressure jump at the trailing edge to the point that the one at the solid-permeable junction is larger. Hence, for highly enough permeable materials, acoustic emission from other locations within the insert becomes the main contributor to broadband self-noise. For its nonpermeable counterpart, the dominant source moves gradually from the trailing-edge position at low frequencies ( $St_c < 12.5$ ) toward more upstream positions at higher frequencies. Interestingly, the transition from one location to another approximately coincides with the previously reported  $St_c^* = 16$ . This points out that roughness noise exceeds the trailing-edge noise contribution from this nondimensional frequency on, in agreement with the results presented in Sec. III. At higher frequencies ( $St_c^* > 16$ ), the two inserts manufactured with  $d_c = 800$   $\mu\text{m}$  foam emit from similar locations. These findings also support roughness as the main cause for high-frequency excess noise, with other secondary mechanisms contributing to the small differences in the scattered sound levels.

For the permeable  $d_c = 450$   $\mu\text{m}$  foam insert, contrary to the most permeable foam, dominant noise emission lies at the trailing edge up to  $St_c = 10$ , where it moves upstream. Discrepancies in the location of the main low-frequency emission between the two permeable treatments indicate that the permeability of a trailing-edge insert is indeed related to the acoustic impedance jumps created by the permeable treatment. It, therefore, seems that, for lower permeability materials, the actual edge scatters sound more efficiently than other regions along the insert, thus becoming the main contributor to the overall low-frequency noise emission; however, for higher permeability treatments, the acoustic impedance jump created more upstream is larger. Following the optimized porous media proposed in Ref. 82, this result suggests that inserts with increasing permeability along the streamwise direction would distribute the acoustic impedance jump along the insert, further reducing the scattered

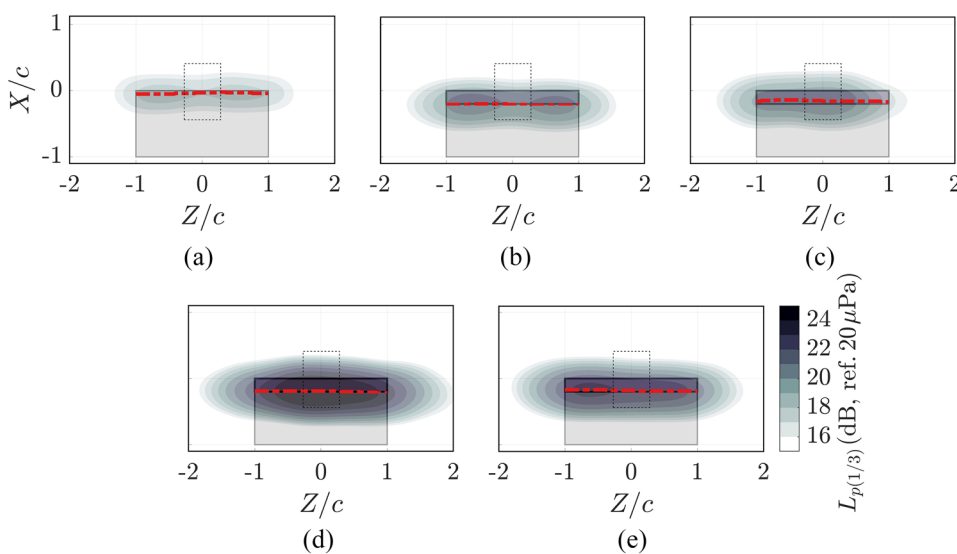
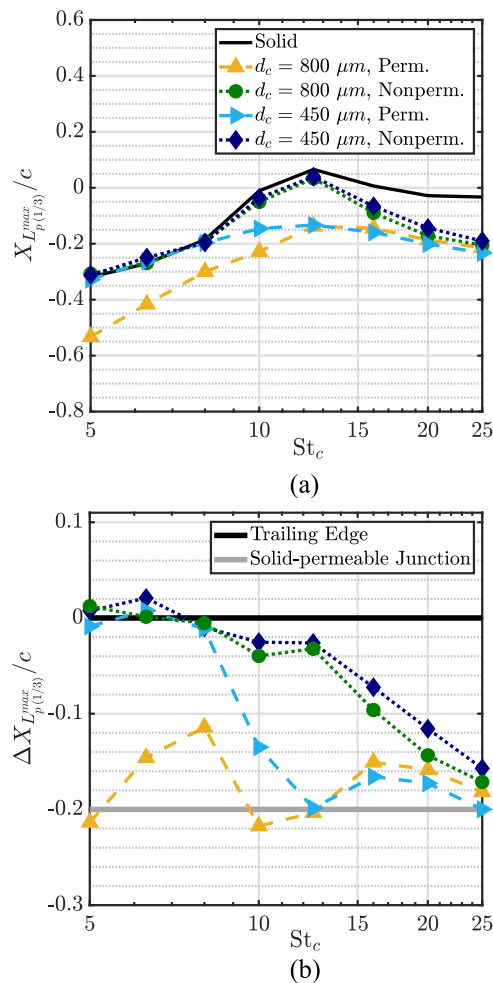


FIG. 16. Source maps for the one-third octave band with  $f_c = 2000$  Hz ( $St_c = 20$ ) for the three test cases. Legend as in Fig. 15.



**FIG. 17.** Streamwise location of the maximum  $L_{p(1/3)}$  in the source maps with respect to the solid case. (a) Absolute coordinates. (b) Coordinates relative to the location of the solid edge.

noise. These observations are also supported by the change in the slope of the low-frequency acoustic spectra, reported in Sec. III only for the permeable  $d_c = 800 \mu m$  foam insert. Spectra for the permeable  $d_c = 450 \mu m$  foam insert and the baseline configuration have approximately the same slope within the frequency range where noise is emitted from the trailing-edge. For the permeable  $d_c = 450 \mu m$  foam insert, the lower permeability of the material is not enough to promote dominant low-frequency scattering from locations other than the trailing edge, and besides the reduction of unsteady pressure mismatch, noise abatement might be partially caused by a decrease in turbulent kinetic energy within the boundary layer.<sup>33</sup> For the  $d_c = 800 \mu m$  foam insert, the higher permeability causes the main noise emission to occur upstream the trailing edge; for this reason, hydrodynamic quantities measured above the edge are inconsistent with the reported noise scattering, as reported in previous experimental work.<sup>25</sup>

## VI. CONCLUSION

Aerodynamic and acoustic measurements on a NACA 0018 airfoil with solid and porous trailing-edge inserts covering 20% of the chord length are carried out. Permeable porous inserts are manufactured employing metal foams with different permeability values. To further assess the effect of the permeability, two nonpermeable counterparts are also manufactured by applying a solid membrane in the symmetry plane. Noise source localization and far-field spectra measurements are performed by means of a phased microphone array. Time-resolved planar PIV measurements are performed to study the flow field around the inserts.

Far-field noise spectra show up to 7 and 10 dB noise attenuation with respect to the solid trailing edge below  $St_c^*$  equal to 20 and 16 for inserts with increasing permeability. Conversely, nonpermeable metal foam and solid inserts produce similar far-field noise scattering below these  $St_c^*$ . Above the  $St_c^*$ , permeable and nonpermeable treatments increase noise with respect to the baseline case, confirming that the excess noise is due to roughness. Yet, the most permeable insert generates additional noise (up to 2 dB) with respect to its nonpermeable equivalent, whereas the least permeable insert has the opposite behavior.

The appearance of cross-flow is confirmed by cross-correlating low-frequency wall-normal velocity fluctuations within the measured domain; this analysis reveals near-wall regions of correlated flow at upper and lower sides of the airfoil only for the permeable inserts. This phenomenon evidences a communication process that affects flow at both sides of the trailing edge, reducing the acoustic impedance jump at the edge (hence sound generation). Contrarily, at higher frequencies, where noise increase with respect to the baseline configuration is reported, velocity fluctuations are not correlated.

As a consequence, changes in the dominant sound emission location within porous treatments are detected in the noise source maps. At lower frequencies, the most permeable insert scatters noise mainly from upstream the trailing edge, while the least permeable insert emits from the edge. The permeability of the treatment thus determines the magnitude of the acoustic impedance jumps created along the metal foam treatment, defining where the scattering of wall-pressure waves into acoustic pressure perturbations is more efficient, in agreement with analytical models<sup>24</sup> and numerical results.<sup>23</sup> Above the  $St_c^*$ , main noise emission occurs upstream the trailing edge independently of the porous insert. Consequently, surface roughness is confirmed as the main contributor to high-frequency excess noise; yet, additional noise generation mechanisms, such as interference between sources present along the insert or/and unsteady injection/ejection of flow, might account for small differences in excess noise between permeable and nonpermeable inserts.

These findings demonstrate the significant role of the cross-flow for broadband self-noise attenuation using permeable materials at the trailing-edge. They also suggest that permeable trailing-edge treatments with a streamwise permeability gradient might overcome the performance of homogeneous porous materials, in line with previous numerical research,<sup>82</sup> as it might allow us to create treatments with a gradual dampening of the pressure mismatch. Further analysis on these aspects, as well as on the phenomena contributing to the high-frequency noise increase, will be addressed in future research.

## ACKNOWLEDGMENTS

The authors are thankful for the assistance of G.R.A.S. and National Instruments to the preparation of the measurement setup. We would also like to thank Dr. J. A. Poulis for his support in the manufacturing of the models subject to study. This research is within the X-FRIS framework of the Delft University of Technology and it did not receive extra funding from agencies in the public, commercial, or not-for-profit sectors.

## REFERENCES

- <sup>1</sup>J. E. Ffowcs-Williams and L. H. Hall, "Aerodynamic sound generation by turbulent flow in the vicinity of a scattering half plane," *J. Fluid Mech.* **40**(04), 657 (1970).
- <sup>2</sup>M. S. Howe, "The influence of vortex shedding on the generation of sound by convected turbulence," *J. Fluid Mech.* **76**(4), 711–740 (1976).
- <sup>3</sup>S. Wagner, R. Bareiß, and G. Guidati, *Wind Turbine Noise* (Springer Berlin Heidelberg, Berlin, Heidelberg, 1996), ISBN: 978-3-642-88712-3.
- <sup>4</sup>S. Oerlemans, P. Sijtsma, and B. M. López, "Location and quantification of noise sources on a wind turbine," *J. Sound Vib.* **299**, 869 (2007).
- <sup>5</sup>E. B. Tingey and A. Ning, "Trading off sound pressure level and average power production for wind farm layout optimization," *Renewable Energy* **114**, 547–555 (2017).
- <sup>6</sup>M. Gruber, P. Joseph, and T. Chong, "On the mechanisms of serrated airfoil trailing edge noise reduction," in *17th AIAA/CEAS Aeroacoustics Conference (32nd AIAA Aeroacoustics Conference)*, June (American Institute of Aeronautics and Astronautics, Reston, Virginia, 2011), pp. 1–23, ISBN: 978-1-60086-943-3.
- <sup>7</sup>D. J. Moreau and C. J. Doolan, "Noise-reduction mechanism of a flat-plate serrated trailing edge," *AIAA J.* **51**(10), 2513–2522 (2013).
- <sup>8</sup>T. P. Chong and A. Vathylakis, "On the aeroacoustic and flow structures developed on a flat plate with a serrated sawtooth trailing edge," *J. Sound Vib.* **354**, 65–90 (2015).
- <sup>9</sup>F. Avallone, S. Pröbsting, and D. Ragni, "Three-dimensional flow field over a trailing-edge serration and implications on broadband noise," *Phys. Fluids* **28**(11), 117101 (2016).
- <sup>10</sup>P. Kholodov and S. Moreau, "Optimization of serrations for broadband trailing-edge noise reduction using an analytical model," in *25th AIAA/CEAS Aeroacoustics Conference*, May (American Institute of Aeronautics and Astronautics, Delft, The Netherlands, 2019), pp. 1–18, ISBN: 978-1-62410-588-3.
- <sup>11</sup>F. Avallone, W. C. P. van der Velden, D. Ragni, and D. Casalino, "Noise reduction mechanisms of sawtooth and combed-sawtooth trailing-edge serrations," *J. Fluid Mech.* **848**, 560–591 (2018).
- <sup>12</sup>A. Finez, M. Jacob, E. Jondeau, and M. Roger, "Broadband noise reduction with trailing edge brushes," in *16th AIAA/CEAS Aeroacoustics Conference* (AIAA, 2010), pp. 1–13.
- <sup>13</sup>M. Herr and W. Dobrzynski, "Experimental investigations in low-noise trailing edge design," *AIAA J.* **43**(6), 1167–1175 (2005).
- <sup>14</sup>I. A. Clark, "Bio-inspired control of roughness and trailing edge noise bio-inspired control of roughness and trailing edge noise," Ph.D. thesis, Virginia Polytechnic Institute and State University, 2017.
- <sup>15</sup>T. Gerhard, S. Erbslöh, and T. Carolus, "Reduction of airfoil trailing edge noise by trailing edge blowing," *J. Phys.: Conf. Ser.* **524**(1), 012123 (2014).
- <sup>16</sup>M. Szoke, D. Fisceletti, and M. Azarpeyvand, "Effect of inclined transverse jets on trailing-edge noise generation," *Phys. Fluids* **30**(8), 085110 (2018).
- <sup>17</sup>T. Geyer and E. Sarraj, "Noise generation by porous airfoils," *13th AIAA/CEAS Aeroacoustics Conference* (AIAA, 2007).
- <sup>18</sup>A. Vathylakis, T. P. Chong, and P. F. Joseph, "Poro-Serrated trailing-edge devices for airfoil self-noise reduction," *AIAA J.* **53**(11), 3379–3394 (2015).
- <sup>19</sup>S. Moreau, P. Laffay, A. Idier, and N. Atalla, "Several noise control of the trailing-edge noise of a controlled-diffusion airfoil," in *22nd AIAA/CEAS Aeroacoustics Conference* (AIAA, 2016), pp. 1–13.
- <sup>20</sup>T. Geyer, E. Sarraj, and C. Fritzsche, "Measurement of the noise generation at the trailing edge of porous airfoils," *Exp. Fluids* **48**(2), 291–308 (2010).
- <sup>21</sup>M. Herr, K. S. Rossignol, J. Delfs, N. Lippitz, and M. Mößner, "Specification of porous materials for low-noise trailing-edge applications," in *20th AIAA/CEAS Aeroacoustics Conference* (AIAA, 2014), pp. 1–19.
- <sup>22</sup>T. Geyer and E. Sarraj, "Trailing edge noise of partially porous airfoils," in *20th AIAA/CEAS Aeroacoustics Conference* (AIAA, 2014).
- <sup>23</sup>J. Delfs, B. Faßmann, N. Lippitz, M. Lummer, M. Mößner, L. Müller, K. Rurkowska, and S. Uphoff, "SFB 880: Aeroacoustic research for low noise take-off and landing," *CEAS Aeronaut. J.* **5**(4), 403–417 (2014).
- <sup>24</sup>A. Kisil and L. J. Ayton, "Aerodynamic noise from rigid trailing edges with finite porous extensions," *J. Fluid Mech.* **836**, 117–144 (2018).
- <sup>25</sup>T. Geyer, E. Sarraj, and C. Fritzsche, "Porous airfoils: Noise reduction and boundary layer effects," *Int. J. Aeroacoust.* **9**(6), 787–820 (2010).
- <sup>26</sup>M. Roger and S. Moreau, "Back-scattering correction and further extensions of Amiet's trailing-edge noise model. Part 1: Theory," *J. Sound Vib.* **286**(3), 477–506 (2005).
- <sup>27</sup>M. Herr and J. Reichenberger, "Search of airworthy trailing-edge noise reduction means," in *17th AIAA/CEAS Aeroacoustics Conference*, June (AIAA, 2011), pp. 5–8, ISBN: 978-1-60086-943-3.
- <sup>28</sup>A. R. Carpio, F. Avallone, D. Ragni, M. Snellen, and S. van der Zwaag, "3D-printed perforated trailing edges for broadband noise abatement," in *25th AIAA/CEAS Aeroacoustics Conference*, May (AIAA, 2019), pp. 1–13.
- <sup>29</sup>J. W. Jaworski and N. Peake, "Aerodynamic noise from a poroelastic edge with implications for the silent flight of owls," *J. Fluid Mech.* **723**(2013), 456–479 (2013).
- <sup>30</sup>J. H. M. Gooden, "Experimental low-speed aerodynamic characteristics of the Wortmann FX66-S-196 V1 airfoil," in *XVI OSTIV Congress* (International Scientific and Technical Soaring Organisation, Chateauroux, France, 1978), pp. 1–11.
- <sup>31</sup>M. Roger and S. Moreau, "Trailing edge noise measurements and prediction for subsonic loaded fan blades," in *8th AIAA/CEAS Aeroacoustics Conference & Exhibit* (AIAA, 2002), Vol. 2460, pp. 1–15.
- <sup>32</sup>S. Moreau, M. Henner, G. Iaccarino, M. Wang, and M. Roger, "Analysis of flow conditions in freejet experiments for studying airfoil self-noise," *AIAA J.* **41**(10), 1895–1905 (2003).
- <sup>33</sup>A. R. Carpio, R. Merino-Martínez, F. Avallone, D. Ragni, M. Snellen, and S. van der Zwaag, "Experimental characterization of the turbulent boundary layer over a porous trailing edge for noise abatement," *J. Sound Vib.* **443**, 537–558 (2019).
- <sup>34</sup>S. Luesutthiviboon, A. Malgouezar, M. Snellen, P. Sijtsma, and D. Simons, "Improving source discrimination performance by using an optimized acoustic array and adaptive high-resolution CLEAN-SC beamforming," in *7th Berlin Beamforming Conference*, 2018.
- <sup>35</sup>P. Welch, "The use of fast fourier transform for the estimation of power spectra: A method based on time averaging over short, modified periodograms," *IEEE Trans. Audio Electroacoust.* **15**(2), 70–73 (1967).
- <sup>36</sup>S. Oerlemans and P. Sijtsma, "Determination of absolute levels from phased array measurements using spatial source coherence," in *8th AIAA/CEAS Aeroacoustics Conference & Exhibit*, June (American Institute of Aeronautics and Astronautics, Reston, Virginia, 2002), pp. 1–12, ISBN: 978-1-62410-119-9, URL: <http://arc.aiaa.org/doi/abs/10.2514/6.2002-2464>.
- <sup>37</sup>P. Sijtsma, "Phased array beamforming applied to wind tunnel and fly-over tests," Technical Report NLR-TP-2010-549, NLR, October 2010.
- <sup>38</sup>T. J. Mueller, *Aeroacoustic Measurements* (Springer, Berlin, New York, 2002), ISBN: 978-3-662-05058-3.
- <sup>39</sup>Lord Rayleigh, "Investigations in optics, with special reference to the spectro-scope," *Philos. Mag. Ser.* **5**(49), 8, 261–274 (1879).
- <sup>40</sup>S. Oerlemans and P. Migliore, "Aeroacoustic wind tunnel tests of wind turbine airfoils," in *10th AIAA/CEAS Aeroacoustics Conference* (AIAA, 2004), pp. 1–18, ISSN 2229-7928, URL: <http://arc.aiaa.org/doi/10.2514/6.2004-3042>.
- <sup>41</sup>E. Sarraj, G. Herold, P. Sijtsma, R. M. Martínez, T. F. Geyer, C. J. Bahr, R. Porteous, D. Moreau, and C. J. Doolan, "A microphone array method benchmarking exercise using synthesized input data," in *23rd AIAA/CEAS Aeroacoustics Conference*, June (American Institute of Aeronautics and Astronautics, 2017), pp. 1–16, ISBN: 978-1-62410-504-3.

- <sup>42</sup>D. Ragni, B. W. Van Oudheusden, and F. Scarano, "3D pressure imaging of an aircraft propeller blade-tip flow by phase-locked stereoscopic PIV," *Exp. Fluids* **52**(2), 463–477 (2012).
- <sup>43</sup>R. J. Adrian, "Particle-imaging techniques for experimental fluid mechanics," *Annu. Rev. Fluid Mech.* **23**, 261–304 (1991).
- <sup>44</sup>M. Raffel, C. E. Willert, and J. Kompenhans, *Particle Image Velocimetry* (Springer Berlin Heidelberg, 1998).
- <sup>45</sup>J. Westerweel, "Fundamentals of digital particle image velocimetry," *Meas. Sci. Technol.* **8**(12), 1379–1392 (1997).
- <sup>46</sup>F. Scarano and M. Riethmuller, "Advances in iterative multigrid PIV image processing," *Exp. Fluids* **29**, 51–60 (2000).
- <sup>47</sup>J. Soria, "Multigrid approach to cross-correlation digital PIV and HPIV analysis," in *13th Australasian Fluid Mechanics Conference, December* (Australasian Fluid Mechanics Society, Melbourne, 1998), pp. 381–384, ISBN: 0732620449.
- <sup>48</sup>F. Scarano, "Iterative image deformation methods in PIV," *Meas. Sci. Technol.* **13**(1), R1–R19 (2001).
- <sup>49</sup>J. Westerweel and F. Scarano, "Universal outlier detection for PIV data," *Exp. Fluids* **39**(6), 1096–1100 (2005).
- <sup>50</sup>A. Melling, "Tracer particles and seeding for particle image velocimetry," *Meas. Sci. Technol.* **8**(12), 1406–1416 (1997).
- <sup>51</sup>B. Wieneke, "PIV uncertainty quantification from correlation statistics," *Meas. Sci. Technol.* **26**(7), 074002 (2015).
- <sup>52</sup>C. A. León, R. Merino-Martínez, D. Ragni, F. Avallone, and M. Snellen, "Boundary layer characterization and acoustic measurements of flow-aligned trailing edge serrations," *Exp. Fluids* **57**(12), 182 (2016).
- <sup>53</sup>F. Avallone, W. C. P. van der Velden, and D. Ragni, "Benefits of curved serrations on broadband trailing-edge noise reduction," *J. Sound Vib.* **400**, 167–177 (2017).
- <sup>54</sup>D. Ragni and C. Ferreira, "Effect of 3D stall-cells on the pressure distribution of a laminar NACA64-418 wing," *Exp. Fluids* **57**(8), 127 (2016).
- <sup>55</sup>M. Drela, "XFOIL: An analysis and design system for low Reynolds number airfoils," in *Low Reynolds Number Aerodynamics: Proceedings of the Conference Notre Dame, Indiana, USA, 5–7 June 1989* (Springer Berlin Heidelberg, Berlin, Heidelberg, 1989), pp. 1–12, ISBN: 978-3-642-84010-4.
- <sup>56</sup>R. J. Moffat, "Describing the uncertainties in experimental results," *Exp. Therm. Fluid Sci.* **1**(1), 3–17 (1988).
- <sup>57</sup>P. R. Spalart and J. H. Watmuff, "Experimental and numerical study of a turbulent boundary layer with pressure gradients," *J. Fluid Mech.* **249**(1), 337 (1993).
- <sup>58</sup>F. H. Clauser, "The turbulent boundary layer," in *Advances in Applied Mechanics* (Elsevier, 1956), pp. 1–51.
- <sup>59</sup>H. Schlichting and K. Gersten, *Boundary-Layer Theory* (Springer Berlin Heidelberg, Berlin, Heidelberg, 2017), Vol. 20, ISBN: 978-3-662-52917-1.
- <sup>60</sup>K. A. Flack and M. P. Schultz, "Roughness effects on wall-bounded turbulent flows," *Phys. Fluids* **26**(10), 101305 (2014).
- <sup>61</sup>J. B. Barlow, W. H. Rae, and A. Pope, *Low-Speed Wind Tunnel Testing*, 3rd ed. (Wiley, 1999), ISBN: 0471557749.
- <sup>62</sup>V. Patil, J. Finn, X. He, R. Ziazi, S. V. Apte, J. A. Liburdy, and B. Wood, "Experimental versus computational methods in the study of flow in porous media," in *Volume 1D, Symposia* (ASME, 2014), pp. 1–9, ISBN: 978-0-7918-4624-7.
- <sup>63</sup>J. Jiménez, "Coherent structures in wall-bounded turbulence," *J. Fluid Mech.* **842**, P1 (2018).
- <sup>64</sup>D. M. Chase, "Sound radiated by turbulent flow off a rigid half-plane as obtained from a wavevector spectrum of hydrodynamic pressure," *J. Acoust. Soc. Am.* **52**(3B), 1011–1023 (1972).
- <sup>65</sup>O. Stalnov, P. Chaitanya, and P. F. Joseph, "Towards a non-empirical trailing edge noise prediction model," *J. Sound Vib.* **372**, 50–68 (2016).
- <sup>66</sup>W. K. Blake, *Mechanics of Flow-Induced Sound and Vibration* (Elsevier Science Publishing Co, Inc, 2017), Vol. 2, ISBN: 9780128092743.
- <sup>67</sup>R. K. Amiet, "Acoustic radiation from an airfoil in a turbulent stream," *J. Sound Vib.* **41**(4), 407–420 (1975).
- <sup>68</sup>B. André, T. Castelain, and C. Bailly, "Investigation of the mixing layer of under-expanded supersonic jets by particle image velocimetry," *Int. J. Heat Fluid Flow* **50**, 188–200 (2014).
- <sup>69</sup>M. Kamruzzaman, T. Lutz, A. Ivanov, A. Herrig, W. Wuerz, and E. Kraemer, "Evaluation of measured anisotropic turbulent two-point correlation data for the accurate prediction of the turbulence noise sources," in *15th AIAA/CEAS Aeroacoustics Conference* (American Institute of Aeronautics and Astronautics, 2009).
- <sup>70</sup>M. Kamruzzaman, T. Lutz, A. Herrig, and E. Krämer, "Semi-Empirical modeling of turbulent anisotropy for airfoil self-noise predictions," *AIAA J.* **50**(1), 46–60 (2012).
- <sup>71</sup>M. Kamruzzaman, Th. Lutz, W. Würz, W. Z. Shen, W. J. Zhu, M. O. L. Hansen, F. Bertagnolio, and H. Aa. Madsen, "Validations and improvements of airfoil trailing-edge noise prediction models using detailed experimental data," *Wind Energy* **15**(1), 45–61 (2012).
- <sup>72</sup>L. Jones, R. Sandberg, and N. Sandham, "Investigation and prediction of transitional airfoil self-noise," in *15th AIAA/CEAS Aeroacoustics Conference, May* (AIAA, 2009), pp. 1–13.
- <sup>73</sup>W. J. Devenport, D. L. Grissom, W. N. Alexander, B. S. Smith, and S. A. L. Glegg, "Measurements of roughness noise," *J. Sound Vib.* **330**(17), 4250–4273 (2011).
- <sup>74</sup>P. Bradshaw, "'Inactive' motion and pressure fluctuations in turbulent boundary layers," *J. Fluid Mech.* **30**(2), 241–258 (1967).
- <sup>75</sup>S. Hoyas and J. Jiménez, "Scaling of the velocity fluctuations in turbulent channels up to  $Re_\tau = 2003$ ," *Phys. Fluids* **18**(1), 011702 (2006).
- <sup>76</sup>Y. Wu and K. T. Christensen, "Spatial structure of a turbulent boundary layer with irregular surface roughness," *J. Fluid Mech.* **655**, 380–418 (2010).
- <sup>77</sup>S. A. S. Ali, M. Azarpeyvand, and C. R. I. Da Silva, "Trailing-edge flow and noise control using porous treatments," *J. Fluid Mech.* **850**, 83–119 (2018).
- <sup>78</sup>J. L. Lage, "The fundamental theory of flow through permeable media from Darcy to turbulence," in *Transport Phenomena in Porous Media* (Elsevier, 1998), pp. 1–30.
- <sup>79</sup>J. Hald and J. J. Christensen, "A novel beamformer array design for noise source location from intermediate measurement distances," *J. Acoust. Soc. Am.* **112**(5), 2448 (2002).
- <sup>80</sup>T. F. Brooks, D. S. Pope, and M. A. Marcolini, "Airfoil self-noise and prediction," Technical Report NASA RP-1218, NASA Langley Research Center, 1989.
- <sup>81</sup>P. A. Nelson, "Noise generated by flow over perforated surfaces," *J. Sound Vib.* **83**(1), 11–26 (1982).
- <sup>82</sup>J. Schulze and J. Sesterhenn, "Optimal distribution of porous media to reduce trailing edge noise," *Comput. Fluids* **78**, 41–53 (2013).